Available online at website: https://journal.bcrec.id/index.php/bcrec

Bulletin of Chemical Reaction Engineering & Catalysis, 20 (3) 2025, 458-470

Original Research Article

Investigation of Ar/CH_4 Mixtures in Dielectric Barrier Discharge: A Simulation Approach for Hydrogen Production

Nedjar Yahia Mohamed Amine*, Mostefaoui Mohamed, Benyoucef Djilali

Laboratory of Electrical Engineering and Renewable Energy (LGEER), Electrical Engineering Department, Faculty of Technology, Hassiba Benbouali University of Chlef, Algeria.

Received: 10th February 2025; Revised: 9th June 2025; Accepted: 10th June 2025
Available online: 19th June 2025; Published regularly: October 2025

Abstract

This modeling study aimed to simulate hydrogen production through dielectric barrier discharge (DBD) in an argon-methane mixture at atmospheric pressure. Argon was selected as an additive due to its high ionization potential, which is expected to facilitate methane dissociation and enhance plasma reactivity. A series of simulations were conducted to assess the impact of varying argon concentrations (ranging from 0% to 90%) on hydrogen generation. A one-dimensional fluid model was employed to investigate methane conversion within the DBD reactor. This approach enabled a comprehensive evaluation of the effects of different Ar/CH_4 ratios, including pure methane, on reactor performance and key plasma characteristics, such as electron density, ion density, and species concentrations. The findings revealed that increasing the argon content significantly enhanced the ionization rate of methane and increased the discharge current, which directly correlated with higher electron density. Moreover, methane conversion efficiency and hydrogen production were found to be strongly dependent on the Ar/CH_4 ratio, with the highest hydrogen yield observed at a 50:50 argon-to-methane mixture.

Keywords: Dielectric barrier discharge; fluid model; methane conversion; Hydrogen; plasma

How to Cite: Amine, N. Y. M., Mohamed, M., Djilali, B. (2025). Investigation of Ar/CH_4 Mixtures in Dielectric Barrier Discharge: A Simulation Approach for Hydrogen Production. *Bulletin of Chemical Reaction Engineering & Catalysis*, 20 (3), 458-470. (doi: 10.9767/bcrec.20352)

Permalink/DOI: https://doi.org/10.9767/bcrec.20352

1. Introduction

Hydrogen is one of most important renewable energy sources, with its use as major element in fuel cell to generate electricity [1], and fuel cell electric vehicle [2]. One of common challenge that faced by researchers is finding efficient sources to produce hydrogen [3]. Among this process, non-thermal plasma is a promising technology that has attracted attention due its ability of converting methane gas to hydrogen whether using microwave plasma reactor, or radio frequency reactor, or dielectric barrier discharge reactor [4-6]. Specifically, Dielectric barrier discharge (DBD) is a recognized plasma technology known for its efficacy in producing reactive species at atmospheric pressure. Its capacity to promote chemical reactions without requiring excessive temperatures or pressures makes it an invaluable asset in numerous industrial applications [7-11].

Dielectric barrier discharge (DBD) is a type of non-thermal plasma generated when a high voltage is applied between two parallel electrodes covered with a dielectric layer [12]. In DBD reactors, methane is commonly used for hydrogen production, as its molecular structure allows for efficient carbon bond dissociation, leading to the formation of hydrogen and various hydrocarbons [13]. Additionally, methane is among the most prevalent gases and a primary component of

* Corresponding Author.
Email: y.nedjar@univ-chlef.dz (N.Y.M. Amine)

natural gas [14]. Research on hydrogen production from methane conversion using dielectric barrier discharge (DBD) plasma has focused on various approaches. Studies on methane cracking in DBD catalytic plasma reactors have identified novel methane utilization pathways while optimizing CH_4 conversion, energy efficiency, and hydrogen selectivity [15]. Other investigations have explored the integration of DBD plasma with NiO/ γ -Al_2O_3 catalysts for methane reforming, examining the effects of different operational parameters on catalyst performance [16].

Numerical simulations are essential for gaining deeper insights into the physical and chemical processes occurring within the discharge gap contributing the optimization and enhanced performance of dielectric barrier discharge (DBD) reactors. Kinetic modeling has been employed to simulate the behavior of DBD reactors operating with methane at atmospheric pressure, offering a deeper understanding of the mechanisms involved in the non-oxidative coupling of methane [17]. Additionally, studies have examined the effect of gas temperature distribution in DBD plasma reactors using pure methane, revealing that higher gas temperatures enhance hydrogen production [18].

The addition of noble gases to the gas mixture in dielectric barrier discharge (DBD) systems plays a crucial role in enhancing hydrogen production and influencing plasma characteristics. Investigations into methane conversion in planar DBD reactors with helium, neon, and argon have demonstrated that argon is the most effective in generating excited and ionized species [19]. Further studies on methane activation confirm that the choice of noble gas has a substantial impact on the efficiency of conversion processes [20]. Additionally, numerical modeling has been employed to analyze DBD behavior in CH_4/O_2 and CH_4/CO_2 gas mixtures, revealing that syngas, higher hydrocarbons, and oxygenates are key reaction products [21]. Experimental studies on methane conversion in non-thermal plasma DBD reactors have also indicated that adding 10% nitrogen enhances hydrogen production [22]. However, despite significant advancements in methane conversion using dielectric barrier discharge (DBD) plasma, several limitations remain. One major challenge is achieving high hydrogen yield while minimizing byproducts due to limited selectivity. The complex plasma dynamics involved in methane activation are not yet fully understood, and the precise role of noble gases in enhancing conversion efficiency requires further investigation.

The objective of this study is to investigate the conversion of methane using dielectric barrier discharge (DBD) plasma, with a particular focus on optimizing hydrogen production and understanding the key factors influencing the process. Specifically, it aims to analyze the effects of Argon gas additives on plasma characteristics and methane dissociation efficiency, providing insights into their role in enhancing hydrogen yield. A one-dimensional fluid model employed to explore the complex plasma dynamics such as electron density, electrical characteristics, and chemical reaction mechanisms caused by the presence of argon. The model incorporates detailed plasma chemistry, accounting for over 100 reactions, including neutral-neutral, ion-neutral, and electron impact reactions.

2. Materials and Methods

2.1 Model Equations

The behavior of electrons in a DBD is described by continuity equations that account for their density and energy. The electron density governed by [23]:

$$\frac{\partial n_e}{\partial t} + \nabla \Gamma_e = R_e \tag{1}$$

with n_e is the electron density, $\boldsymbol{\Gamma}_e$ is the electron flux vector, and R_e denotes the source term accounting for processes such as ionization and attachment.

The electron flux is typically expressed using the drift-diffusion approximation:

$$\Gamma_e = V_e n_e = -\mu_e n_e E - \nabla n_e D_e \tag{2}$$

where μ_e D_e and E refer to electron mobility, electron diffusivity and the electric field respectively.

The electron energy density is described by an energy balance equation:

$$\frac{\partial n_\varepsilon}{\partial t} + \nabla \Gamma_\varepsilon + E\Gamma_e = R_\varepsilon \tag{3}$$

$$\Gamma_\varepsilon = -\mu_\varepsilon n_\varepsilon E - \nabla n_\varepsilon D_\varepsilon \tag{4}$$

where ε refer to energy, n_ε to electron energy density, Γ_ε is the mean energy flux, R_ε is the electron energy loss or gain in collision, μ_ε and D_ε are the electron energy mobility and electron energy diffusivity.

The mean electron energy was calculated across this expression:

$$\varepsilon = \frac{n_\varepsilon}{n_e} \tag{5}$$

The electron energy loss obtained by summing the collisional energy loss over all reactions:

$$R_\varepsilon = \sum_{j=1}^{P} x_j k_j N_n n_e \Delta\varepsilon_j \tag{6}$$

with x_j mole fraction of the target species for reaction j, k_j rate coefficient for reaction j, N_n total

neutral number density, $\Delta\varepsilon_j$ energy loss from reaction j, and P refer to inelastic electron-neutral collisions.
The electric field is computed using the following equation:

$$\nabla\, \varepsilon_0 . \varepsilon_r \nabla V = \rho_s \quad (7)$$

where V refers to the electrostatic potential, ε_r is the relative permittivity, and ε_0 is the vacuum permittivity, and ρ is the space charge density.
The space charge density ρ is computed automatically according to the plasma chemical defined in the model, utilizing the formula:

$$\rho_s = q(\sum_{k=1}^{N} Z_k n_k - n_e) \quad (8)$$

with Z_k is the electric charge, q is the absolute value of electronic charge.
The properties of the dielectric given by this relation:

$$D = \varepsilon_0 . \varepsilon_r E \quad (9)$$

with D refer to the electric field displacement.

2.2 Boundary Conditions

The dielectric surfaces that are adjacent to the opening where the plasma forms are subject to surface charge accumulation as a result of the following boundary condition:

$$-n\,.\,(D_1 - D_2) = \rho_s \quad (10)$$
$$\frac{d\rho_s}{dt} = n \cdot J_i + n \cdot J_e \quad (11)$$

where ρ_s is surface charge density, D_1 and D_2 refer to the electric field displacement, $n \cdot J_i$ is the total ion current density at the walls (boundary 0, 1, Figure 1), and $n \cdot J_e$ is the total electron current density at the walls (boundary 0, 1, Figure 1).

2.3 Electric Potential

An applied voltage of 5100 V powers this model at a high frequency of 10 kHz under atmospheric pressure and a gas temperature of 300 K.

$$Vrf = 5100.sin(2.\pi.f) \quad (12)$$

2.4 Initial Value

The initial electron density represents a small number of seed electrons present within the discharge gap domain (Figure 1): $n_{e,0}$=10^6 (1/m^3), initial mean electron energy: $\mathcal{E}$= 5(V).

2.5 Time-Stepping Method

An implicit time integration scheme based on the Backward Differentiation Formula (BDF) used to address the stiffness of the governing equations. The simulation employed an adaptive time-stepping strategy, with the initial time step set to 1×10^{-11} s. The solver dynamically adjusted the step size to accurately resolve the rapid transient behavior during breakdown and relaxation phases.

2.6 Spatial Discretization and Mesh

The simulation domain, corresponding to a 1 mm discharge gap, was discretized into 200 uniform spatial nodes. This mesh density was selected based on mesh sensitivity analysis to capture steep gradients in plasma parameters, particularly near dielectric boundaries.

2.7 Solver Configuration and Convergence Criteria

The nonlinear algebraic system resulting from temporal and spatial discretization was solved using a fully coupled Newton-Raphson iteration. Within each iteration, the linear system was handled using an efficient iterative solver with appropriate preconditioning to ensure robustness and speed (Relative tolerance: 1×10^{-4}; Absolute tolerance: 1×10^{-12}) and a maximum of 50 nonlinear iterations was allowed per time step. Convergence was assessed based on the residual norm of the solution variables and conservation of charge within the domain.

2.9 Description of Model Geometry

To model the process, a one-dimensional configuration was developed, consisting of two parallel plates coated with a dielectric material having a relative permittivity of εr=10 and a thickness of 2 mm. The discharge gap, measuring 1 mm, was filled with a mixture of argon and methane, as depicted in Figure 1.

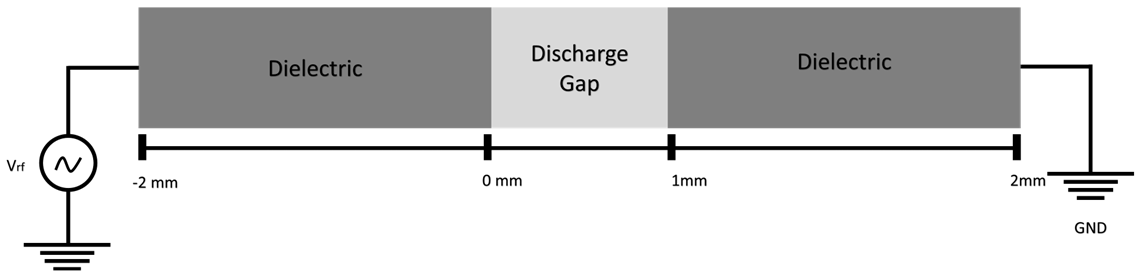

Figure 1. 1D geometry model of dielectric barrier discharge reactor

2.10 Plasma Chemistry

This study utilizes a chemistry model that includes a thorough array of species, such as electrons, ions, radicals, and neutrals, as well as more than 100 related processes. The electron impact reactions of methane are presented in Table 1 [24], whereas the interaction between argon and methane is described in Table 2. Methane reactions and their respective rate coefficients are presented in Table 3.

3. Results and Discussion

This section presents the numerical simulation results for the dielectric barrier discharge (DBD) plasma operated under various argon – methane gas mixtures. To ensure model credibility, simulations were initially performed using Ar/CH_4 mixtures with 5% and 10% methane concentrations. These conditions were selected to match experimentally relevant configurations and allow comparison with known discharge behavior.

Figure 2 presents the discharge current waveforms of the dielectric barrier discharge (DBD) in Ar/CH_4 mixture (5% Ar, 95% CH_4) over one period, as predicted by the 1D fluid model and compared to the experimental results reported in [36]. The simulated waveform leads the experimental measurement by approximately 4 μs, which is consistent with the solver's 0.5 μs temporal resolution and the idealized nature of the model, which neglects circuit response and energy losses. Despite this minor temporal shift, the model successfully reproduces the overall shape and peak structure of the discharge current. The simulated peak current (0.097 mA) deviates by less than 3% from the experimentally measured value (0.10 mA).

Figure 3 shows the distribution of ions, electrons, and different species across the discharge gap which are taken at the peak current (t = 30 μs). According to the figure, we can notice an increase in the density number of ions in the vicinity of the anode where it is clear that the most

Table 1. Electron impact reactions with methane.

No.	Formula	Type	Δε (eV)	Ref.
R_1	$e + CH_4 \Rightarrow e + CH_4$	Elastic	0	[24]
R_2	$e + CH_4 \Rightarrow e + CH_4$	Excitation	0.162	[24]
R_3	$e + CH_4 \Rightarrow e + CH_4$	Excitation	0.362	[24]
R_4	$e + CH_4 \Rightarrow e + CH_3 + H$	Excitation	8.8	[24]
R_5	$e + CH_4 \Rightarrow e + CH_2 + H_2$	Excitation	9.4	[24]
R_6	$e + CH_4 \Rightarrow e + CH + H_2 + H$	Excitation	12.5	[24]
R_7	$e + CH_4 \Rightarrow e + C + H_2 + H_2$	Excitation	14	[24]
R_8	$e + CH_4 \Rightarrow 2e + CH_4^+$	Ionization	12.63	[24]
R_9	$e + CH_4 \Rightarrow 2e + H + CH_3^+$	Ionization	14.25	[24]
R_{10}	$e + CH_4 \Rightarrow 2e + H_2 + CH_2^+$	Ionization	15.1	[24]
R_{11}	$e + CH_4 \Rightarrow 2e + H + H_2 + CH^+$	Ionization	19.9	[24]
R_{12}	$e + CH_4 \Rightarrow 2e + H_2 + H_2 + C^+$	Ionization	19.6	[24]
R_{13}	$e + CH_4 \Rightarrow 2e + CH_2 + H_2^+$	Ionization	20.1	[24]
R_{14}	$e + CH_4 \Rightarrow 2e + CH_3 + H^+$	Ionization	18	[24]

Table 2. Reactions argon-methane with rate coefficient.

No.	Reaction	Rate coefficient	Ref
R_1	$Ar^+ + CH_4 \Rightarrow CH_3^+ + H + Ar$	6.32×10^7 m^3/(s.mol)	[25]
R_2	$Ar^* + CH_4 \Rightarrow Ar + CH_2 + 2H$	1.98×10^8 m^3/(s.mol)	[25]
R_3	$Ar^* + CH_4 \Rightarrow Ar + CH + H + H_2$	3.49×10^7 m^3/(s.mol)	[25]
R_4	$Ar^* + CH_4 \Rightarrow Ar + CH_3 + H$	3.49×10^7 m^3/(s.mol)	[25]
R_5	$Ar + CH_3 + H \Rightarrow CH_4 + Ar$	2.97×10^7 m^6/(s.mol^2)	[26]
R_7	$Ar + C_2H + H \Rightarrow C_2H_2 + Ar$	11243 m^6/(s.mol^2)	[26]
R_9	$Ar + C_2H_2 + H \Rightarrow C_2H + H_2 + Ar$	3.1878×10^5 m^6/(s.mol^2)	[26]
R_{10}	$Ar + C_2H_3 \Rightarrow C_2H_2 + H + Ar$	7.82×10^5 m^3/(s.mol)	[26]
R_{11}	$Ar^+ + CH_4 \Rightarrow CH_3^+ + H + Ar$	6.32×10^7 m^3/(s.mol)	[25]
R_{12}	$Ar^+ + H_2 \Rightarrow Ar^+ + H_2$	1.636×10^8 m^3/(s.mol)	[27]
R_{13}	$Ar^+ + C_2H_2 \Rightarrow C_2H_2^+ + Ar$	25.29×10^7 m^3/(s.mol)	[27]
R_{14}	$Ar^* + Ar^* \Rightarrow e + Ar + Ar^+$	3.3734×10^7 m^3/(s.mol)	[35]
R_{15}	$Ar^* + Ar \Rightarrow Ar + Ar$	1807	[35]

Table 3. Reactions with rate coefficient.

N	Reaction	Rate Coefficient			Ref
		A [m^3/s.mol]	E [J/mol]	n	
R_1	$CH_4 + CH_2 \Rightarrow CH_3 + CH_3$	0.0713E − 16	41988	0	[28]
R_2	$CH_4 + CH \Rightarrow C_2H_4 + H$	153E − 16		−0.9	[29]
R_3	$CH_4 + H \Rightarrow CH_3 + H_2$	2.2E − 26	33632	3	[30]
R_4	$CH_3 + CH_3 \Rightarrow C_2H_6$	4.66E − 16		−0.37	[28]
R_5	$CH_3 + CH_3 \Rightarrow C_2H_4 + H_2$	170E − 16	133030		[29]
R_6	$CH_3 + CH_3 \Rightarrow C_2H_5 + H$	0.5E − 16	56540		[28]
R_7	$CH_3 + CH_2 \Rightarrow C_2H_4 + H$	0.7E − 16			[28]
R_8	$CH_3 + CH \Rightarrow C_2H_3 + H$	0.5E − 16			[29]
R_9	$CH_3 + C \Rightarrow C_2H_2 + H$	0.83E − 16			[29]
R_{10}	$CH_3 + H2 \Rightarrow CH_4 + H$	1.1E − 26	39410	2.74	[29]
R_{11}	$CH_3 + H \Rightarrow CH_2 + H_2$	1E − 16	63190		[28]
R_{12}	$CH_2 + CH_2 \Rightarrow C_2H_4$	0.017E − 16			[32]
R_{13}	$CH_2 + CH_2 \Rightarrow C_2H_2 + 2H$	1.8E − 16	3326		[29]
R_{14}	$CH_2 + CH_2 \Rightarrow C_2H_2 + H_2$	26.3E − 16	50000		[29]
R_{15}	$CH_2 + CH_2 \Rightarrow CH_3 + CH$	4E − 16	41572		[29]
R_{16}	$CH2 + CH \Rightarrow C_2H_2 + H$	0.66E − 16			[31]
R_{17}	$CH_2 + C \Rightarrow C_2H + H$	0.83E − 16			[31]
R_{18}	$CH_2 + H_2 \Rightarrow CH_3 + H$	0.19E − 16	53212	0.17	[29]
R_{19}	$CH_2 + H \Rightarrow CH + H_2$	2.2E − 16			[29]
R_{20}	$CH + CH \Rightarrow C_2H_2$	2E − 16			[28]
R_{21}	$CH + C \Rightarrow C_2 + H$	0.66E − 16			[29]
R_{22}	$CH + H_2 \Rightarrow CH_2 + H$	5.46E − 16	16155		[29]
R_{23}	$CH + H \Rightarrow C + H_2$	1.31E − 16	665		[28]
R_{24}	$C + H_2 \Rightarrow CH + H$	6.64E − 16	97278		[28]
R_{25}	$CH_4^+ + CH_4 \Rightarrow CH_5^+ + CH_3$	11.5E − 16			[32]
R_{26}	$CH_4^+ + H2 \Rightarrow CH_5^+ + H$	1.086E − 16	−300	−0.14	[29]
R_{27}	$CH_4^+ + H \Rightarrow CH_3^+ + H_2$	0.1E − 16			[29]
R_{28}	$CH_5^+ + CH_2 \Rightarrow CH_3^+ + CH_4$	9.6E − 16			[29]
R_{29}	$CH_5^+ + CH \Rightarrow CH_2^+ + CH_4$	120E − 16		−0.5	[29]
R_{30}	$CH_5^+ + C \Rightarrow CH^+ + CH_4$	12E − 16			[29]
R_{31}	$CH_5^+ + H \Rightarrow CH_4^+ + H_2$	1.5E − 16			[29]
R_{32}	$CH_3^+ + CH_4 \Rightarrow C_2H_5^+ + H_2$	9.6E − 16			[32]
R_{33}	$CH_3^+ + CH_2 \Rightarrow C_2H_3^+ + H_2$	9.9E − 16			[29]
R_{34}	$CH_3^+ + CH \Rightarrow C_2H_2^+ + H_2$	123E − 16		−0.5	[29]
R_{35}	$CH_3^+ + C \Rightarrow C_2H^+ + H_2$	12E − 16			[29]
R_{36}	$CH_3^+ + H \Rightarrow CH_2^+ + H_2$	7E − 16	87800		[29]
R_{37}	$CH_2^+ + CH_4 \Rightarrow C_2H_5^+ + H$	2.88E − 16			[29]
R_{38}	$CH_2^+ + CH_4 \Rightarrow C_2H_4^+ + H_2$	5E − 16			[29]
R_{39}	$CH_2^+ + CH_4 \Rightarrow C_2H_3^+ + H_2 + H$	2.64E − 16			[29]
R_{40}	$CH_2^+ + CH_4 \Rightarrow C_2H_2^+ + 2H_2$	1.44E − 16			[29]
R_{41}	$CH_2^+ + C \Rightarrow C_2H^+ + H$	12E − 16			[29]
R_{42}	$CH_2^+ + H_2 \Rightarrow CH_3^+ + H$	7.2E − 16			[33]
R_{43}	$CH_2^+ + H \Rightarrow CH^+ + H_2$	10E − 16	58866		[29]
R_{44}	$CH^+ + CH_4 \Rightarrow C_2H_4^+ + H$	0.77E − 16			[29]
R_{45}	$CH^+ + CH_4 \Rightarrow C_2H_3^+ + H_2$	10.57E − 16			[29]
R_{46}	$CH^+ + CH_4 \Rightarrow C_2H_2^+ + H_2 + H$	1.55E − 16			[29]
R_{47}	$CH^+ + CH_2 \Rightarrow C_2^+ + H_2$	10E − 16			[29]
R_{48}	$CH^+ + CH \Rightarrow C_2^+ + H_2$	128E − 16		−0.5	[29]
R_{49}	$CH^+ + C \Rightarrow C_2^+ + H$	12E − 16			[29]
R_{50}	$CH^+ + H_2 \Rightarrow CH_2^+ + H$	10.1E − 16			[29]
R_{51}	$CH^+ + H \Rightarrow C^+ + H_2$	74.75E − 16	241	−0.37	[29]
R_{52}	$C^+ + CH_4 \Rightarrow C_2H_3^+ + H$	10.3E − 16			[29]
R_{53}	$C^+ + CH_4 \Rightarrow C_2H_2^+ + H_2$	4.2E − 16			[29]

R_{54}	$C^+ + CH_3 \Rightarrow C_2H_2^+ + H$	13E − 16			[29]
R_{55}	$C^+ + CH_3 \Rightarrow C_2H^+ + H_2$	10E – 16			[34]
R_{56}	$C^+ + CH_2 \Rightarrow C_2H^+ + H$	5.2E − 16			[29]
R_{57}	$C^+ + CH_2 \Rightarrow CH_2^+ + C$	5.2E – 16			[29]
R_{58}	$C^+ + CH \Rightarrow C_2^+ + H$	65.8E − 16		−0.5	[29]
R_{59}	$C^+ + CH \Rightarrow CH^+ + C$	65.8E − 16		−0.5	[29]
R_{60}	$C^+ + H2 \Rightarrow CH^+ + H$	1E − 16	38579		[29]
R_{61}	$H_2^+ + CH_4 \Rightarrow CH_4^+ + H_2$	14E − 16			[29]
R_{62}	$H_2^+ + CH_4 \Rightarrow CH_5^+ + H$	1.1E − 16			[29]
R_{63}	$H_2^+ + CH_4 \Rightarrow CH_3^+ + H_2 + H$	22.8E − 16			[29]
R_{64}	$H_2^+ + CH_2 \Rightarrow CH_2^+ + H_2.$	10E − 16			[29]
R_{65}	$H_2^+ + CH_2 \Rightarrow CH_3^+ + H$	10E – 16			[29]
R_{66}	$H_2^+ + CH \Rightarrow CH^+ + CH_2$	123E − 16		−0.5	[29]
R_{67}	$H_2^+ + CH \Rightarrow CH_2^+ + H$	123E – 16		−0.5	[29]
R_{68}	$H_2^+ + C \Rightarrow CH^+ + H$	24E – 16			[29]
R_{69}	$H_2^+ + H_2 \Rightarrow H_3^+ + H$	21E − 16			[29]
R_{70}	$H_2^+ + H \Rightarrow H^+ + H_2$	6.4E − 16			[29]
R_{71}	$H^+ + CH_4 \Rightarrow CH_4^+ + H$	15.2E − 16			[29]
R_{72}	$H^+ + CH_4 \Rightarrow CH_3^+ + H_2$	22.8E – 16			[29]
R_{73}	$H^+ + CH_3 \Rightarrow CH_3^+ + H$	34E – 16			[29]
R_{74}	$H^+ + CH_2 \Rightarrow CH_2^+ + H$	14E − 16			[29]
R_{75}	$H^+ + CH_2 \Rightarrow CH^+ + H_2$	14E – 16			[29]
R_{76}	$H^+ + CH \Rightarrow CH^+ + H$	329E − 16		−0.5	[29]
R_{77}	$C_2H_4^+ + H \Rightarrow C_2H_3^+ + H2$	3E – 16			[29]
R_{78}	$CH_4 + C_2H_3 \Rightarrow C_2H_4 + CH_3$	2.41E – 30	22860	4.02	[29]
R_{79}	$CH_3 + C_2H_6 \Rightarrow C_2H_5 + CH_4$	0.9E − 30	34670	4	[29]
R_{80}	$CH_3 + C_2H_5 \Rightarrow C_2H_4 + CH_4$	0.019E − 16			[28]
R_{81}	$CH_3 + C_2H_3 \Rightarrow C_2H_2 + CH_4$	8833E – 16	2494	−1.5	[28]
R_{82}	$CH_2 + C_2H_3 \Rightarrow C_2H_2 + CH_3$	0.3E − 16			[28]
R_{83}	$CH + C_2H_6 \Rightarrow C_2H_4 + CH_3$	4.8E − 16	242.7	−0.52	[29]
R_{84}	$H + C_2H_5 \Rightarrow C_2H_6$	0.6E − 16			[30]
R_{85}	$H + C_2H_5 \Rightarrow CH_3 + CH_3$	0.6E − 16			[29]
R_{86}	$H + C_2H_5 \Rightarrow C_2H_4 + H_2$	0.03E − 16			[32]
R_{87}	$H + C_2H_4 \Rightarrow C_2H_5$	0.14E − 20	4150	1.49	[33]
R_{88}	$H + C_2H_4 \Rightarrow C_2H_3 + H_2$	2.2E – 24	51220	2.53	[33]
R_{89}	$H + C_2H_3 \Rightarrow C_2H_2 + H_2$	0.332E – 16			[28]
R_{90}	$H + C_2H_2 \Rightarrow C_2H + H_2$	3.8E – 16	113359		[29]
R_{91}	$C_2H_5 + C_2H_5 \Rightarrow C_2H_6 + C_2H_4$	0.024E − 16			[29]
R_{92}	$C_2H_5 + C_2H_5 \Rightarrow C_4H_{10}$	0.19E − 16			[29]
R_{93}	$C_2H_5 + C_2H \Rightarrow C_2H_4 + C_2H_2$	0.03E − 16			[28]
R_{94}	$CH_4^+ + C_2H_6 \Rightarrow C_2H_4^+ + CH_4 + H_2$	19.1E − 16			[28]
R_{95}	$CH_4^+ + C_2H_4 \Rightarrow C_2H_4^+ + CH_4$	13.8E − 16			[28]
R_{96}	$CH_4^+ + C_2H_4 \Rightarrow C_2H_5^+ + CH_3$	4.23E − 16			[33]
R_{97}	$CH_4^+ + C_2H_2 \Rightarrow C_2H_2^+ + CH_4$	11.3E − 16			[29]
R_{98}	$CH_4^+ + C_2H_2 \Rightarrow C_2H_3^+ + CH_3$	12.3E − 16			[29]
R_{99}	$CH_5^+ + C_2H_4 \Rightarrow C_2H_5^+ + CH_4$	15E − 16			[29]
R_{100}	$CH_5^+ + C_2H_2 \Rightarrow C_2H_3^+ + CH_4$	16E − 16			[29]
R_{101}	$CH_5^+ + C_2H \Rightarrow C_2H_2^+ + CH_4$	9E − 16			[29]
R_{102}	$CH_3^+ + C_2H_6 \Rightarrow C_2H_5^+ + CH_4$	14.8E − 16			[29]
R_{103}	$CH_3^+ + C_2H_4 \Rightarrow C_2H_3^+ + CH_4$	3.5E − 16			[29]
R_{104}	$CH_3^+ + C_2H_3 \Rightarrow C_2H_3^+ + CH_3$	51.9E − 16		−0.5	[29]
R_{105}	$H_2^+ + C_2H_6 \Rightarrow C_2H_6^+ + H_2$	2.94E – 16			[29]
R_{106}	$H_2^+ + C_2H_6 \Rightarrow C_2H_5^+ + H_2 + H$	13.7E − 16			[29]
R_{107}	$H_2^+ + C_2H_6 \Rightarrow C_2H_4^+ + 2H_2$	23.5E − 16			[29]
R_{108}	$H_2^+ + C_2H_6 \Rightarrow C_2H_3^+ + 2H_2 + H$	6.86E – 16			[29]
R_{109}	$H_2^+ + C_2H_6 \Rightarrow C_2H_2^+ + 3H_2$	1.96E − 16			[29]

R_{110}	$H_2^+ + C_2H_4 \Rightarrow C_2H_4^+ + H_2$	22.1E − 16	[30]
R_{111}	$H_2^+ + C_2H_4 \Rightarrow C_2H_3^+ + H_2 + H$	18.1E − 16	[30]
R_{112}	$H_2^+ + C_2H_4 \Rightarrow C_2H_2^+ + 2H_2$	8.8E – 16	[29]
R_{113}	$H_2^+ + C_2H_2 \Rightarrow C_2H_2^+ + H_2$	48.2E − 16	[29]
R_{114}	$H_2^+ + C_2H_2 \Rightarrow C_2H_3^+ + H$	4.8E − 16	[29]
R_{115}	$H^+ + C_2H_6 \Rightarrow C_2H_4^+ + H_2 + H$	14E − 16	[29]
R_{116}	$H^+ + C_2H_6 \Rightarrow C_2H_3^+ + 2H_2$	28E – 16	[29]
R_{117}	$H^+ + C_2H_5 \Rightarrow C_2H_4^+ + H_2$	16.5E − 16.	[29]
R_{118}	$H^+ + C_2H_5 \Rightarrow C_2H_3^+ + H_2 + H$	30.6E – 16	[29]
R_{119}	$H^+ + C_2H_4 \Rightarrow C_2H_3^+ + H_2$	30E – 16	[29]

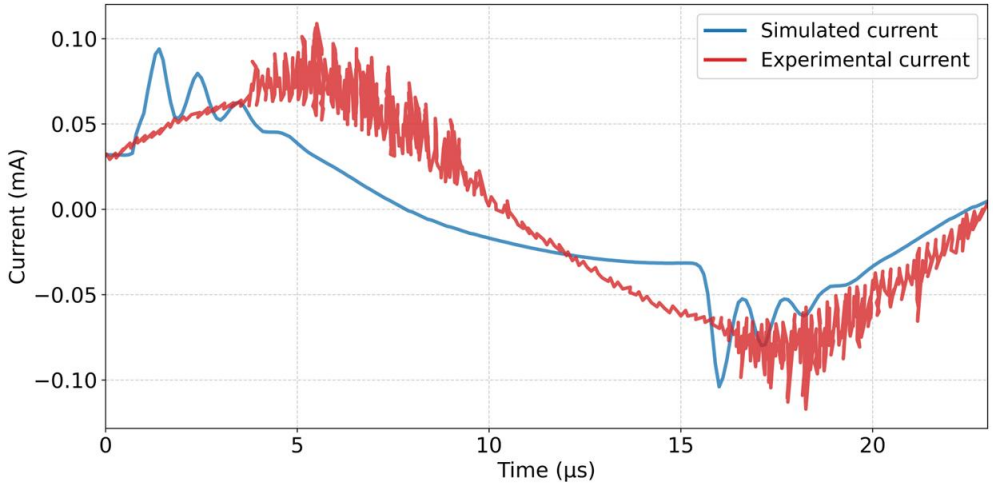

Figure 2. Comparison between simulated and experimental discharge current profiles [36].

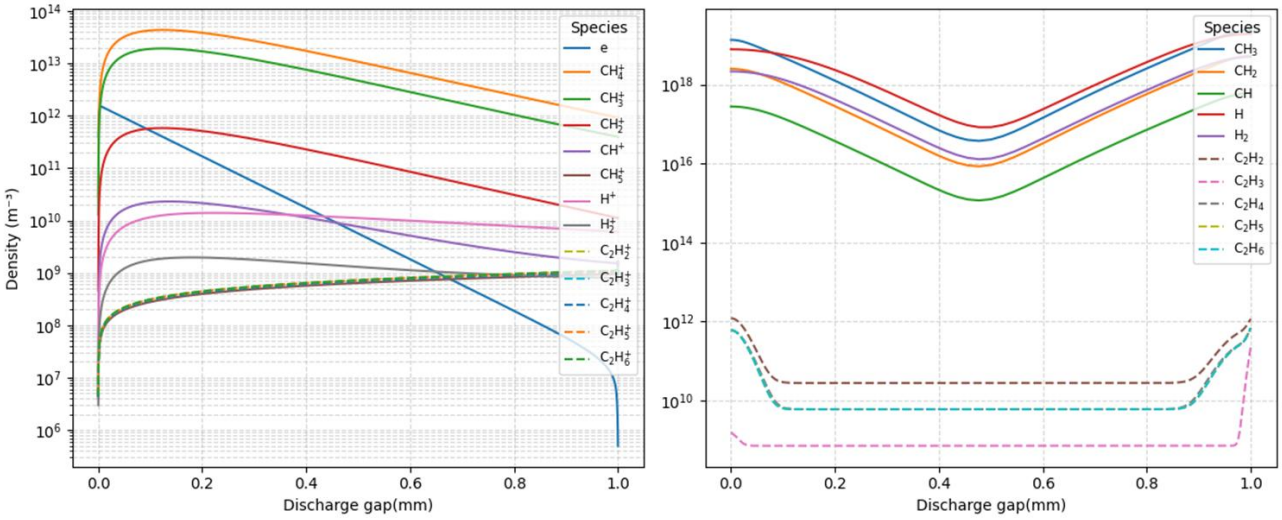

Figure 3. Distribution of ion, electron and different species densities across discharge gap.

abundant ions are (CH_4^+, CH_3^+, CH_2^+, H^+, H_2^+), The result is attributed to the elevated number of electrons near the anode, which collide with neutral species, leading to ion generation and an increase in their density. The number of electrons decreases as they approach closer to the cathode. this is due to their interaction with neutral species and atom, leading to the formation of other species. Furthermore, electron density decreased as migrating toward the ground, which resulted in more collision processes.

The spatial distribution of radicals and molecules across the discharge gap follows a clear sequential pattern. the radical CH_3 appears first, generated by electron-impact dissociation of CH_4 (reaction R4, $\Delta\varepsilon$ = 8.8 eV), reaching its initial peak shortly after the ionization front, consistent with its relatively low excitation threshold. CH_2 produced via R5 ($\Delta\varepsilon$ = 9.4 eV), rises only slightly later. hydrogen atoms (H) from R6 and R7 ($\Delta\varepsilon \approx$ 12.5–14 eV) emerge next, accumulating to higher

densities as the discharge continues. hydrogen (H_2), formed through R5 and secondary pathways (effective $\Delta\varepsilon \geq 9.4$ eV), builds up most slowly, peaking near the cathode. This progression from lower- to higher-energy thresholds confirms that low-energy electron processes dominate early radical formation, whereas higher-energy channels govern the later stages of plasma chemistry, consistent with the findings of previous researcher [34].

Figure 4 presents the temporal evolution of key charged and neutral species alongside the discharge current waveform during a single DBD pulse at the dielectric wall (boundary 0, Figure 1). The discharge current exhibits a distinct peak that correlates with a sharp rise in electron density, primarily due to ionization processes. Among the ionized species, CH_3^+ and CH_3^+ appear early in the discharge, peaking concurrently with the electron density. This rise is attributed to direct electron-impact ionization of methane occurring during the high-field phase. CH_2^+ and CH^+ emerge slightly later and at lower concentrations, followed by hydrogen-based ions (H_2^+ and H^+), which display a similar but slightly delayed trend compared to the carbon-containing ions. The lower densities of these hydrogen ions are consistent with the higher ionization potentials of H_2 (15.4 eV) and H (13.6 eV).

In a complementary view, the second panel of Figure 4 illustrates the evolution of neutral species in alignment with the discharge current. The rapid formation of CH_3 and H radicals shortly after the current peak suggests that these species are predominantly generated through lower-energy dissociation reactions. CH_2 and CH follow similar trends but with lower peak densities, reflecting their higher excitation energy requirements and a greater tendency for recombination.

Effect of Argon Study: in this section, we present a result obtained from a DBD reactor filled with different ratios of argon. Figure 5 illustrates the time evolution of the applied voltage and discharge current in a DBD reactor with varying argon concentrations in methane (from 0% to 90%). The results show that the discharge current exhibits one peak per half-cycle of the applied voltage for all gas ratios. As the argon content increases, the peak current also increases, indicating that argon's higher ionization potential enhances electron generation, leading to stronger current pulses. Furthermore, as the Ar ratio rises, the microdischarge ignites earlier in each half-cycle, shifting the current peak forward in time. The maximum current peak, 0.12 A, occurs at 80% Ar, which is attributed to the increased production of high-energy electrons. At 90% Ar, a slight decrease in peak current is observed due to the reduced methane concentration, which limits further ionization.

Figure 6 illustrates the distribution of electron density across the discharge gap for various Ar/CH_4 mixtures at t = 29.8 µs. As the ratio of argon increases, the electron density increases near the anode compared to pure methane. Notably, at 90% Ar, the electron density reaches 10^{15} m^{-3}, highlighting the influence of argon on the discharge characteristics. However, the electron density profile at 80% Ar is lower than those at 40% and 50% Ar despite its higher inert gas content. This result is attributed to the filamentary nature of the discharge at higher Argon content, where the current waveform exhibits transient spikes. At t = 29.8 µs, the discharge current for the 80% Ar case is in a declining phase, reducing the ionization rate and thus the electron density. In contrast, for 40%, 50%, and 90% Ar cases, the current is still rising at this time, contributing to higher electron densities.

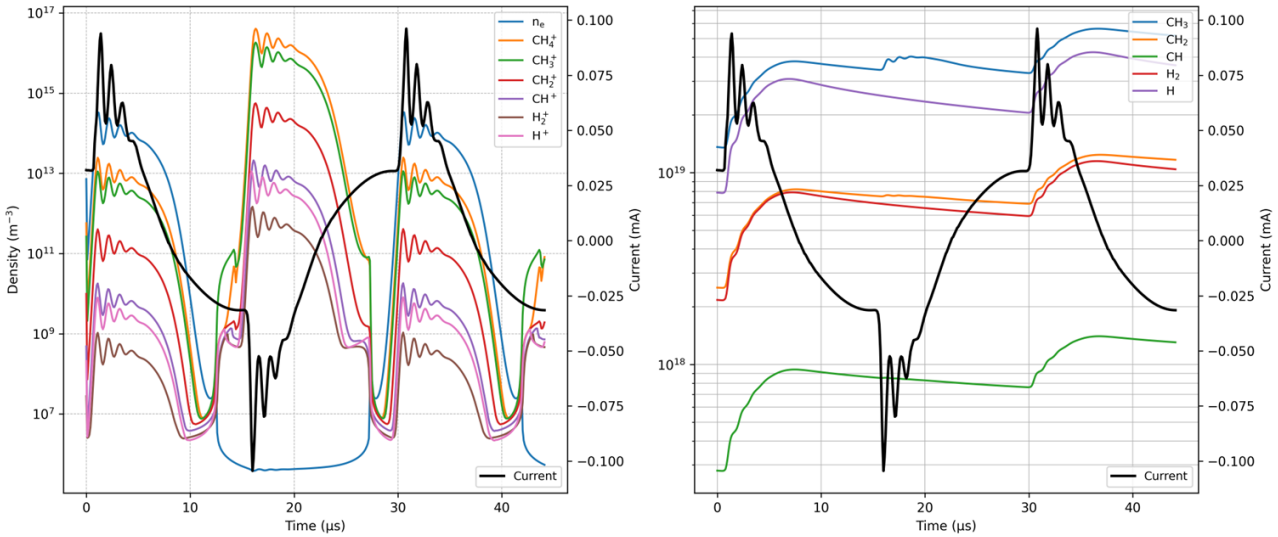

Figure 4. Temporal evolution of charged and neutral species with discharge current.

Figure 7 illustrates the impact of increasing the argon proportion on ion and electron densities, revealing notable variations in the concentrations of key charged species. From the figure, the peak electron density rises steadily with Ar concentration, reflecting argon's higher ionization cross-section and lower energy loss in inelastic collisions. At low Ar levels (0–40%), the densities of CH_3^+, CH_2^+, CH^+, H^+, and H_2^+ all increase, whereas at high Ar fractions (>70%) Ar^+ becomes the dominant ion species. Between 40% and 60% Ar, both electron and ion density curves level off into pronounced plateaus, signaling a balance between ion–molecule reactions and charge-transfer processes.

Figure 8 illustrates the evolution of species densities with varying argon ratios in DBD plasma. As the Ar concentration increases, the densities of hydrocarbon radicals, such as CH_3, CH_2, and CH, exhibit a modest rise, particularly up to around 50% Ar. Among them, CH_3 shows the most significant increase, rising from 1.3×10^{19} m^{-3} to 1.7×10^{19} m^{-3}. Similarly, hydrogen also show an upward trend, with densities increasing

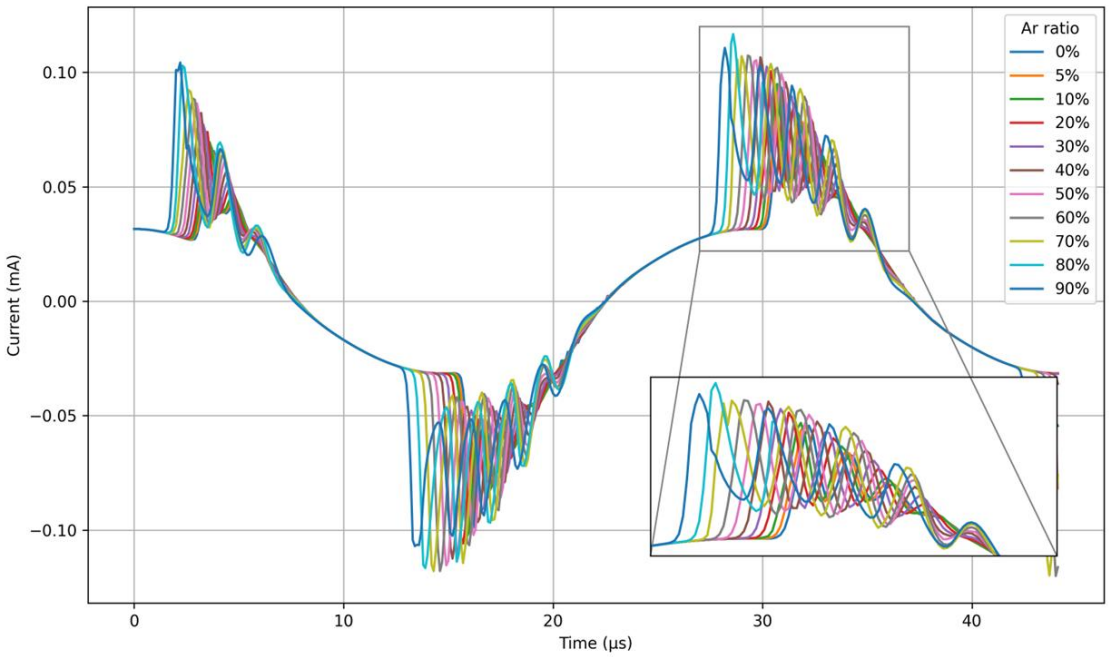

Figure 5. Influence of argon-methane ratios on discharge current.

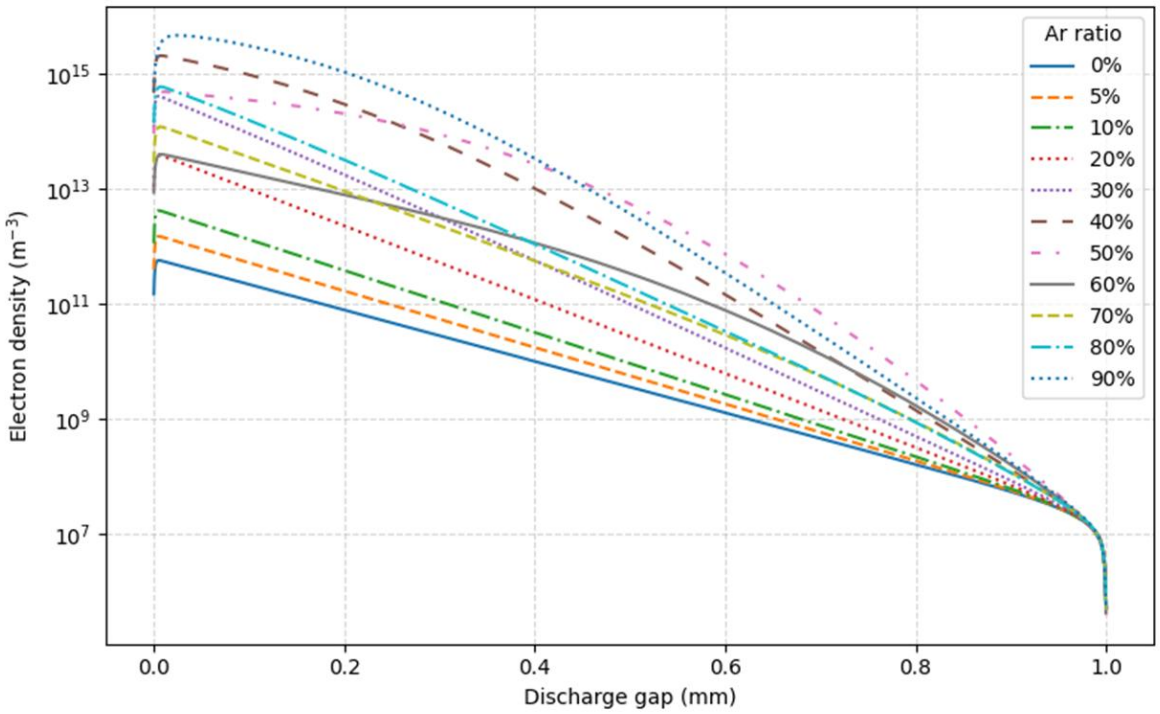

Figure 6. Influence of argon-methane ratio on distribution of electron density across the gap.

from 2.1 × 10^{18} m^{-3} to 3.1 × 10^{18} m^{-3}, indicating optimal conditions for methane dissociation and hydrogen production. The consistent presence of H and H_2 indicates ongoing methane dissociation and hydrogen recombination, which are less sensitive to dilution effects due to their lower mass and higher mobility. These species are primarily produced via fast electron-impact and Ar^+ assisted dissociation reactions, such as R_1 through R_4 in Table 2. These reactions are characterized by relatively high rate constants, on the order of 10^{-17} to 10^{-16} $m^3/(s \cdot mol)$, supporting the formation of radicals even under increasing Ar content. This high reaction efficiency contributes to a quasi-steady-state concentration of CH_x and H species, resulting in the nearly flat or mildly increasing density trends observed before the 50% Ar threshold. Beyond 50% Ar, however, a gradual reduction in radical densities becomes apparent. This decline is attributed to further increases in argon content, which result in a dilution effect, lowering methane concentration and subsequently reducing the formation of hydrogen and other hydrocarbon species. In contrast, Figure 8b shows that stable higher-carbon molecules such as C_2H_2, C_2H_4, and C_2H_6 exhibit different

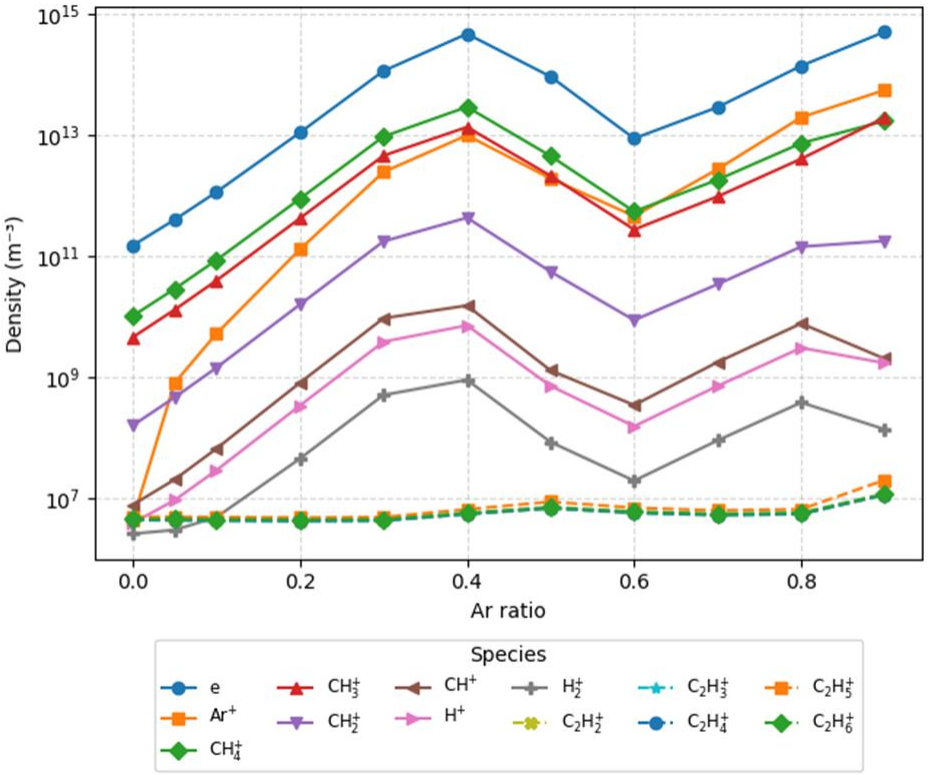

Figure 7. Density of electron, and ion, for different argon-methane ratio.

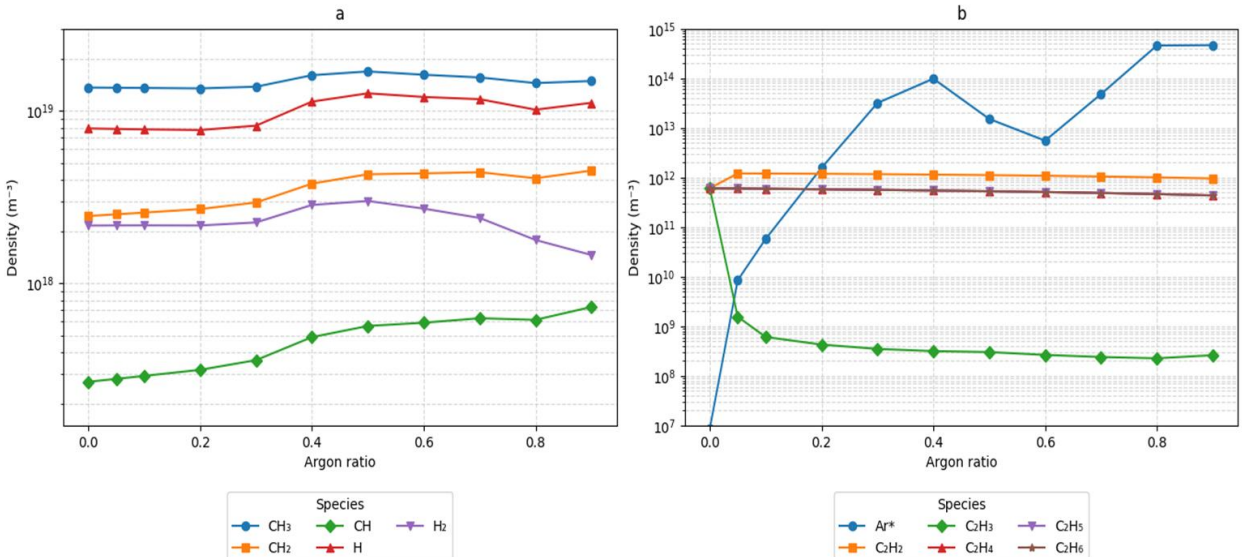

Figure 8. Density of various species at different argon-methane ratios.

behavior. Although their absolute densities remain lower than those of CH_3 and CH_2, they persist throughout the full range of Ar ratios, with a generally declining trend at higher Ar concentrations. These species are primarily formed from neutral-neutral reaction, ion-neutral, and three-body reactions, such as R_9 and R_7 (Table 2), which possess significantly lower rate constants. This reduced reaction efficiency, combined with the increased electron energy from Ar enrichment, favors molecular fragmentation over synthesis leading to the observed suppression of C_2 based species.

4. Conclusion

In this study, a numerical simulation of dielectric barrier discharge in an Ar/CH_4 mixture was conducted to investigate hydrogen production during the discharge process. The model evaluated the influence of the Ar/CH_4 ratio on plasma behavior and species generation. The results indicate that CH_3 is the most abundant radical, while CH_4^+, CH_3^+, and CH_2^+ are the predominant ionic species. Notably, increasing the argon concentration leads to a higher discharge current due to elevated electron density, which enhances methane dissociation and results in greater production of both neutral and ionic species.

Among the most affected species are CH_3, CH_2, H_2, and H, while the primary ions exhibiting substantial density increases include CH_3^+, CH_2^+, CH^+, H^+, and H_2^+. The hydrogen density was found to be sensitive to the gas composition, peaking at 3.1×10^{18} m^{-3} for a 50:50 Ar/CH_4 mixture. These findings provide valuable insights into optimizing plasma conditions for applications such as hydrogen production and hydrocarbon conversion. Beyond gas composition, other aspects of DBD reactor design warrant consideration. The current electrode gap (1 mm) appears sufficient for stable discharge generation, but optimizing this distance could enhance power efficiency and electron energy utilization. Additionally, synchronization between discharge activity and gas residence time may improve methane conversion, particularly during high-current filamentary discharge phases. Although residence time was not directly modeled in this work, future studies should couple plasma kinetics with gas flow dynamics to determine the optimal residence time that maximizes CH_4 conversion.

Future work should also explore multi-dimensional reactor designs, including partially packed bed configurations, the influence of different dielectric material, reduce unwanted byproducts species, and detailed surface chemistry. These insights support the development of more efficient plasma-assisted systems for hydrogen production and methane reforming.

Acknowledgments

The authors gratefully acknowledge the Laboratory of Electrical Engineering and Renewable Energy (LGEER), Faculty of Technology, Hassiba Benbouali University of Chlef, for its valuable support, resources, and research environment throughout this study.

CRedit Author Statement

Author Contributions: Nedjar Yahia Mohamed Amine: Conceptualization, Methodology, Investigation, Software, Data Curation, Writing Original Draft Preparation, Visualization; Mostefaoui Mohamed: Supervision, Writing Review and Editing, Validation, Resources; Benyoucef Djillali: Co-supervision, Project Administration, Writing Review and Editing, Validation. All authors have read and agreed to the published version of the manuscript.

References

[1] Le, T. T., Sharma, P., Bora, B. J., Tran, V. D., Truong, T. H., Le, H. C., Nguyen, P. Q. P. (2024). Fueling the future: A comprehensive review of hydrogen energy systems and their challenges. *International Journal of Hydrogen Energy*, 54, 791–816. DOI: 10.1016/j.ijhydene.2023.08.044

[2] Younas, M., Shafique, S., Hafeez, A., Javed, F., Rehman, F. (2022). An Overview of Hydrogen Production: Current Status, Potential, and Challenges. *Fuel*, 316, 123317. DOI: 10.1016/j.fuel.2022.123317

[3] Xu, Z. (2022). Hydrogen Fuel-cell Technology in Electric Vehicles: Current Usage, Materials and Future Applications. *Highlights in Science, Engineering and Technology*, 17, 20–29. DOI: 10.54097/hset.v17i.2432

[4] Majd Alawi, N., Hung Pham, G., Barifcani, A., Hoang Nguyen, M., & Liu, S. (2019). Syngas formation by dry and steam reforming of methane using microwave plasma technology. *IOP Conference Series: Materials Science and Engineering*, 579(1), 012022. DOI: 10.1088/1757-899X/579/1/012022

[5] Sun, J., & Chen, Q. (2019). Kinetic roles of vibrational excitation in RF plasma assisted methane pyrolysis. *Journal of Energy Chemistry*, 39, 188–197. DOI: 10.1016/j.jechem.2019.01.028

[6] Gang, Y., Long, Y., Wang, K., Zhang, Y., Ren, X., Zhang, H., & Li, X. (2024). Plasma Catalytic Non-Oxidative Conversion of Methane into Hydrogen and Light Hydrocarbons. *Plasma Chemistry and Plasma Processing*. DOI: 10.1007/s11090-024-10497-1

[7] Tański, M., Reza, A., Przytuła, D., & Garasz, K. (2023). Ozone Generation by Surface Dielectric Barrier Discharge. *Applied Sciences*, 13(12), Article 12. DOI: 10.3390/app13127001

[8] Chavan, U., & Patil, S. (2024). Water Treatment Using Atmospheric Pressure Plasma: Dielectric Barrier Discharge and Corona Discharge Method, and Reactive Species Analysis. *E3S Web of Conferences*, 559, 03006. DOI: 10.1051/e3sconf/202455903006

[9] Paw, N. R., Kimura, T., Ishijima, T., Tanaka, Y., Nakano, Y., Uesugi, Y., Sueyasu, S., Watanabe, S., & Nakamura, K. (2021). Surface treatment of titanium dioxide nanopowder using rotary electrode dielectric barrier discharge reactor. *Plasma Science and Technology*, 23(10), 105505. DOI: 10.1088/2058-6272/ac0ed9

[10] Ahlawat, K., Jangra, R., Ish, A., Jain, N., & Prakash, R. (2024). A dielectric barrier discharge based low pressure narrow band far UV-C 222 nm excimer lamp and its efficiency analysis. *Physica Scripta*, 99(2), 025018. DOI: 10.1088/1402-4896/ad1cb9

[11] Zhou, A., Chen, D., Dai, B., Ma, C., Li, P., & Yu, F. (2017). Direct decomposition of CO 2 using self-cooling dielectric barrier discharge plasma. *Greenhouse Gases: Science and Technology*, 7(4), 721–730. DOI: 10.1002/ghg.1683

[12] Kogelschatz, U. (2003). Dielectric-Barrier Discharges: Their History, Discharge Physics, and Industrial Applications. *Plasma Chemistry and Plasma Processing*, 23(1), 1–46. DOI: 10.1023/A:1022470901385

[13] Hameed, S., & Comini, E. (2024). Methane conversion for hydrogen production: Technologies for a sustainable future. *Sustainable Energy & Fuels*, 8(4), 670–683. DOI: 10.1039/D3SE00972F

[14] Akpasi, S.O., Akpan, J.S., Amune, U.O., Olaseinde, A.A., & Kiambi, S.L. (2024). Methane Advances: Trends and Summary from Selected Studies. *Methane*, 3(2), 276–313. DOI: 10.3390/methane3020016

[15] Khoja, A.H., Azad, A.K., Saleem, F., Khan, B.A., Naqvi, S.R., Mehran, M.T., & Amin, N.A.S. (2020). Hydrogen Production from Methane Cracking in Dielectric Barrier Discharge Catalytic Plasma Reactor Using a Nanocatalyst. *Energies*, 13(22), 5921. DOI: 10.3390/en13225921

[16] Song, L., Kong, Y., & Li, X. (2017). Hydrogen production from partial oxidation of methane over dielectric barrier discharge plasma and NiO/γ-Al2O3 catalyst. *International Journal of Hydrogen Energy*, 42(31), 19869–19876. DOI: 10.1016/j.ijhydene.2017.06.008

[17] Maitre, P.-A., Bieniek, M. S., & Kechagiopoulos, P. N. (2021). Modelling excited species and their role on kinetic pathways in the non-oxidative coupling of methane by dielectric barrier discharge. *Chemical Engineering Science*, 234, 116399. DOI: 10.1016/j.ces.2020.116399

[18] Benmoussa, A., Belasri, A., Larouci, B., Belkharroubi, F., & Belmiloud, N. (2022). Gas Temperature Effect in Methane DBD Reactor for Hydrogen Production. *Plasma Medicine*, 12(3), 41–58. DOI: 10.1615/PlasmaMed.2023047179

[19] Jo, S., Hoon Lee, D., Seok Kang, W., & Song, Y.-H. (2013). Methane activation using noble gases in a dielectric barrier discharge reactor. *Physics of Plasmas*, 20(8), 083509. DOI: 10.1063/1.4818795

[20] Jo, S., Hoon Lee, D., & Song, Y.-H. (2015). Product analysis of methane activation using noble gases in a non-thermal plasma. *Chemical Engineering Science*, 130, 101–108. DOI: 10.1016/j.ces.2015.03.019

[21] De Bie, C., van Dijk, J., & Bogaerts, A. (2015). The Dominant Pathways for the Conversion of Methane into Oxygenates and Syngas in an Atmospheric Pressure Dielectric Barrier Discharge. *The Journal of Physical Chemistry C*, 119 (39), 22331–22350. DOI: 10.1021/acs.jpcc.5b06515

[22] Saleem, F., Kennedy, J., Dahiru, U.H., Zhang, K., & Harvey, A. (2019). Methane conversion to H2 and higher hydrocarbons using non-thermal plasma dielectric barrier discharge reactor. *Chemical Engineering and Processing - Process Intensification*, 142, 107557. DOI: 10.1016/j.cep.2019.107557

[23] Hagelaar, G.J.M., & Pitchford, L.C. (2005). Solving the Boltzmann equation to obtain electron transport coefficients and rate coefficients for fluid models. *Plasma Sources Science and Technology*, 14(4), 722–733. DOI: 10.1088/0963-0252/14/4/011

[24] Gadoum, A., & Benyoucef, D. (2019). Set of the Electron Collision Cross Sections for Methane Molecule. *IEEE Transactions on Plasma Science*, 47(3), 1505–1513. DOI: 10.1109/TPS.2018.2885610

[25] Kosarev, I.N., Aleksandrov, N.L., Kindysheva, S.V., Starikovskaia, S.M., & Starikovskii, A. Yu. (2008). Kinetics of ignition of saturated hydrocarbons by nonequilibrium plasma: CH4-containing mixtures. *Combustion and Flame*, 154(3), 569–586. DOI: 10.1016/j.combustflame.2008.03.007

[26] Gordillo-Vázquez, F.J., & Albella, J.M. (2004). Influence of the pressure and power on the non-equilibrium plasma chemistry of C_2, C_2H, C_2H_2, CH_3 and CH_4 affecting the synthesis of nanodiamond thin films from C_2H_2 (1%)/H_2 /Ar-rich plasmas. *Plasma Sources Science and Technology*, 13(1), 50–57. DOI: 10.1088/0963-0252/13/1/007

[27] Denysenko, I.B., Xu, S., Long, J.., Rutkevych, P.P., Azarenkov, N.A., & Ostrikov, K. (2004). Inductively coupled Ar/CH4/H2 plasmas for low-temperature deposition of ordered carbon nanostructures. *Journal of Applied Physics*, 95(5), 2713–2724. DOI: 10.1063/1.1642762

[28] NIST chemical kinetics database. http://kinetcis.nist.gov/kinetics/

[29] The umist database for astrochemistry. http://udfa.ajmarkwick.net/index.php

[30] The kinetic database for astrochemistry. http://kida.astrochem-tools.org

[31] Mao, M., & Bogaerts, A. (2010). Investigating the plasma chemistry for the synthesis of carbon nanotubes/nanofibres in an inductively coupled plasma-enhanced CVD system: The effect of processing parameters. *Journal of Physics D: Applied Physics*, 43(31), 315203. DOI: 10.1088/0022-3727/43/31/315203

[32] Huntress, W.T., Jr. (1977). Laboratory studies of bimolecular reactions of positive ions in interstellar clouds, in comets, and in planetary atmospheres of reducing composition. *The Astrophysical Journal Supplement Series*, 33, 495. DOI: 10.1086/190439

[33] Jaritz, M., Hopmann, C., Behm, H., Kirchheim, D., Wilski, S., Grochla, D., Banko, L., Ludwig, A., Böke, M., Winter, J., Bahre, H., & Dahlmann, R. (2017). Influence of residual stress on the adhesion and surface morphology of PECVD-coated polypropylene. *Journal of Physics D: Applied Physics*, 50(44), 445301. DOI: 10.1088/1361-6463/aa8798

[34] De Bie, C., Verheyde, B., Martens, T., Van Dijk, J., Paulussen, S., & Bogaerts, A. (2011). Fluid Modeling of the Conversion of Methane into Higher Hydrocarbons in an Atmospheric Pressure Dielectric Barrier Discharge. *Plasma Processes and Polymers*, 8(11), 1033–1058. DOI: 10.1002/ppap.201100027

[35] Zhang Zeng-Hui, Zhang Guan-Jun, Shao Xian-Jun, Chang Zheng-Shi, Peng Zhao-Yu, Xu Hao, (2012). Modelling study of dielectric barrier glow discharge in Ar/NH3 mixture at atmospheric pressure. *Acta Physica Sinica*, 61(24), 245205. DOI: 10.7498/aps.61.245205

[36] Barni, R., & Riccardi, C. (2018). Gas-phase evolution of Ar/H2O and Ar/CH4 dielectric barrier discharge plasmas. *The European Physical Journal D*, 72(4), 62. DOI: 10.1140/epjd/e2018-80570-8.